

Mono-lepton Signature of a Neutrino-philic Dark Fermion at Hadron Colliders

Kai Ma^{*} and Lin-Yun He[†]

Faculty of Science, Xi'an University of Architecture and Technology, Xi'an, 710055, China

(Dated: March 3, 2025)

Abstract

Searching for dark matter at high-energy colliders and direct detection experiments can effectively cover nearly the entire mass range from the MeV to the TeV scale. In this paper, we focus on four-fermion contact interactions formulated within the framework of Effective Field Theory. Specifically, we present a detailed analysis of mono-lepton production at the LHC. Our results demonstrate that tensor operators exhibit superior sensitivity in the mono-lepton channel, constraining energy scales up to 3 TeV for a nearly massless dark fermion using current LHC data. Moreover, these operators mediate both spin-independent and spin-dependent absorption processes in nuclear targets. A systematic comparison of constraints between direct detection experiments and collider measurements reveals the LHC's distinct advantage in exploring sub-GeV dark matter candidates while maintaining competitive sensitivity at the TeV scale. Notably, direct detection experiments such as Super-Kamiokande and Borexino achieve complementary constraints in the 10-100 MeV mass range through their unique capabilities: utilization of light nuclei targets, large exposure volumes, and distinctive features of the recoil energy spectra.

^{*} kai@xauat.edu.cn

[†] a1164432527@gmail.com

CONTENTS

I. Introduction	2
II. Effective Operators	4
III. Mono-lepton Production	6
IV. Absorptions at Nuclear Target	12
A. Spin-Independent Absorption	14
B. Spin-Dependent Absorption	16
C. Absorption for the Tensor Operator	19
V. Conclusion	21
A. Experimental Parameters for SI and SD Absorption	21
Acknowledgments	21
References	21

I. INTRODUCTION

For several decades, dark matter (DM) has been acknowledged as an essential and fundamental component of the universe. This recognition is firmly supported by compelling and robust evidence derived from various aspects of galactic dynamics as well as comprehensive cosmological observations, as detailed in references [1–4]. Despite the extensive and intensive efforts in conducting numerous searches, both within the high energy collider searches [5–7] and through astrophysical measurements [8–10], no definitive and conclusive signals of DM have been detected. As a direct consequence, the intrinsic properties of DM remain largely enigmatic and undetermined. This lack of knowledge has spurred the community to continuously explore new experimental techniques and theoretical frameworks in an attempt to unlock the mysteries of DM.

Recent developments have brought the absorption operator of fermionic DM into sharper focus. This operator is intended to shed light on the interactions between the DM and

the Standard Model (SM) particles [11–14], and can be explored in direct detection experiments with various target, such as semiconductors [15], superconductors [16], phonons [17], electrons [18, 19]. The CDEX Collaboration has recently set upper limits on the absorption cross-section of DM with a mass of 5 keV when it interacts with electron targets [20]. For vector interactions, the measured upper bound is $5.5 \times 10^{-46} \text{ cm}^2$ and for axial-vector interactions, it was $1.8 \times 10^{-46} \text{ cm}^2$. The above result impose crucial constraints on both the theoretical models being developed and the experimental approaches being employed to detect and describe the characteristics of DM.

In case of that the DM is stabilised due to an underlying discrete symmetry like \mathbb{Z}_2 , DM particles are usually produced in pairs in collider experiments. In contrast, there is no such symmetry in the absorptive operators. The DM particle can be stable only in case of that it has a low enough mass, such that its decay width can be minimized, and allow it to persist until now as a viable DM candidate with the correct relic abundance [18, 21, 22]. Correspondingly, the collider singles are also completely different. In this paper, we explore the mono-lepton production which has been recognized as a promising channel in searching for missing energy [23–25]. The unique advantage of mono-lepton events lies in their minimal background noise, which significantly enhances the experimental sensitivity to various interaction operators between the dark particle and SM particles.

We look into four-fermion contact interactions within the Effective Field Theory (EFT) framework. We are specifically interested in the interactions that involve a fermionic DM, a neutrino, and two quarks. These effective operators have already been studied quite a lot in earlier works [13, 26–28]. Our analysis is centered on the mono-lepton process. where the outgoing DM and neutrino behaves as missing energy. In addition, we examine the parton-level absorption processes at nuclear targets that are brought about by these four-fermion interactions. We also compare the exclusion limits that come from direct detection experiments and LHC data. By doing this, we can provide useful predictions for future research directions.

The rest of this paper is organized as follows. In Sec. II, we give a short review of the four-fermion contact interactions and the validity of the EFT framework in high energy condition. In Sec. III, we study the production properties of both the signal and the irreducible background of the mono-lepton process. and the constraints from the (future) hadron colliders are also studied. In Sec. IV, we study the absorption process of a light DM on a

nuclei target, both for the spin-independent and spin-dependent scatterings. The combined constraints from the hadron collider searches and direct detections are also discussed. Our conclusions are given in the final section [V](#).

II. EFFECTIVE OPERATORS

At hadron collider, the four-fermion effective operators can be investigated via mono-jet [\[29–31\]](#), mono-photon [\[32–34\]](#), and mono-Z/W processes [\[35–39\]](#) which can be summarized as mono-X processes [\[40–42\]](#). These four-fermion contact interactions can also lead to the absorption of fermionic DM by nuclei [\[43–45\]](#), where the DM mass and energy are transferred to the nuclear recoil energy [\[14, 44, 46, 47\]](#). In the EFT framework, such lowest order interactions are encapsulated by the following dimension-6 operators:

$$\begin{aligned}
\mathcal{O}_S &\equiv (\bar{q}q) (\bar{\nu}_L \chi_R) , \\
\mathcal{O}_P &\equiv (\bar{q}i\gamma_5 q) (\bar{\nu}_L \chi_R) , \\
\mathcal{O}_V &\equiv (\bar{q}\gamma_\mu q) (\bar{\nu}_L \gamma^\mu \chi_L) , \\
\mathcal{O}_A &\equiv (\bar{q}\gamma_\mu \gamma_5 q) (\bar{\nu}_L \gamma^\mu \chi_L) , \\
\mathcal{O}_T &\equiv (\bar{q}\sigma_{\mu\nu} q) (\bar{\nu}_L \sigma^{\mu\nu} \chi_R) ,
\end{aligned} \tag{1}$$

Here, q denotes an isospin doublet, $q = (u \ d)^T$, representing the first generation of quarks. The operators link the quark current with the DM-neutrino current, capturing potential interactions across these fermionic fields. The corresponding effective Lagrangian is expressed as:

$$\mathcal{L}_{\text{eff}} = \sum_i \frac{1}{\Lambda_i^2} \mathcal{O}_i + \text{h.c.} \tag{2}$$

where Λ_i denotes the energy scale associated with each operator. This formalism allows for the systematic exploration of beyond SM physics at accessible large energy scales, examining potential signals and constraints from particle physics experiments and astrophysical observations.

To ensure the integrity of the EFT framework outlined above, several conditions must be met regarding the energy scales and the renormalization group effects. Specifically, the energy scale Λ_i associated with the EFT operators must exceed the energy of the particle collisions involved [\[26\]](#). Furthermore, if a mediator is involved, its mass should be significantly greater than the collision energy to avoid invalidating the EFT approximation [\[48–50\]](#).

Given that our EFT operators are defined at the TeV scale, renormalization group (RG) effects become particularly significant at lower energy scales, such as those encountered during absorption processes [28, 51–56]. These RG effects, due to the lack of Galilean invariance, can lead to a mixing of operators with differing Lorentz structures when applied in non-relativistic scenarios [27]. However, the extent of this mixing effect hinges significantly on the strength of the coupling between DM and the Standard Model fermions, particularly the top quark [27, 28, 51–56].

Furthermore, the dark fermion can decay only through following channel,

$$\chi \rightarrow \nu + q + \bar{q} \quad (3)$$

and the corresponding total decay widths are given as,

$$\begin{aligned} \Gamma_{S/P} &= \frac{m_\chi^5}{1024\pi^3\Lambda_{S/P}^4}, \\ \Gamma_{V/A} &= \frac{m_\chi^5}{256\pi^3\Lambda_{V/A}^4}, \\ \Gamma_T &= \frac{3m_\chi^5}{128\pi^3\Lambda_T^4}, \end{aligned} \quad (4)$$

One can observe that, in general, the total decay widths for all the operators depend on $\frac{m_\chi^5}{\Lambda_i^4}$. If the dark fermion is very light, specifically when $m_\chi < \Lambda_{\text{QCD}}$, the aforementioned decay channels are prohibited because of the quark pair condensation. Conversely, signals of the four-fermion contact couplings may show up in the invisible decay of neutral pion $\pi \rightarrow \nu\bar{\chi}$ [57]. Since there is no direct signal, this channel is very difficult to detect. However, this mass range is outside the range of interest for a light DM (studied in the Sec. IV for direct detections. On the other hand, at a collider with (parton level) center-of-mass energy $\sqrt{\hat{s}}$, the typical decay length of the dark fermion is given as,

$$L_\chi = \gamma_\chi \tau_\chi = \frac{\sqrt{\hat{s}}}{2m_\chi \Gamma_\chi} \left(1 + \frac{m_\chi^2}{\sqrt{\hat{s}}} \right). \quad (5)$$

For a relatively light dark fermion, the following relation holds: $L_\chi \approx \sqrt{\hat{s}}/(2m_\chi \Gamma_\chi)$. As a reference, we simply stipulate that the typical decay length should be greater than 1 m. The Fig. 1 illustrates the regions where $L_\chi < 1$ m for a typical center-of-mass energy at the LHC, which is $\sqrt{\hat{s}} = 1$ TeV. One can observe that for a dark fermion with a mass $m_\chi \lesssim 5$ GeV, the assumption of invisibility is consistently valid. Moreover, for a dark fermion

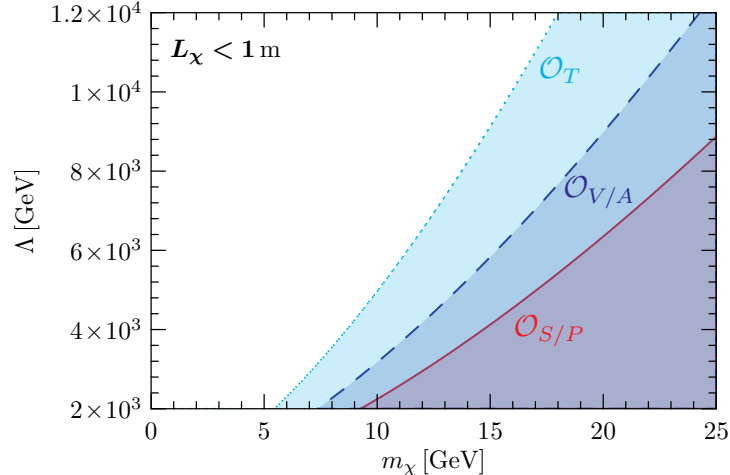


FIG. 1. Typical decay length of the dark fermion in the m_χ - Λ plane. The parton level center of mass energy is chosen as $\sqrt{\hat{s}} = 1\text{TeV}$.

with $m_\chi \lesssim 5\text{GeV}$, there exist various thermal (and non-thermal) production mechanisms that can account for the observed DM relic abundance [57]. In this paper, instead of delving into the details of such production mechanisms, we conduct a study in a model-independent manner on the signal properties in hadron collider and direct detection experiments. For a relatively heavier dark fermion, the restriction regarding invisibility is dependent on the energy scale Λ_i . However, it must be pointed out that this constraint is model-dependent rather than a general one, especially when the dark fermion χ is just one part of an entire dark sector, as referenced in [58–62]. Taking into account the advantage of high-energy colliders, that is, their ability to search for much heavier particles, we will investigate the signals of a dark fermion across the full mass region as long as it is kinematically feasible.

III. MONO-LEPTON PRODUCTION

As we have mentioned, the mono-lepton production serves as a promising channel in collider searches of missing energy. In our case the process can be induced by the four-fermion operators defined in (1), and the parton-level channels are given as,

$$q + \bar{q}' \rightarrow \ell^\pm + \nu + \bar{\nu} + \chi(\bar{\chi}). \quad (6)$$

Here the neutrinos and the dark fermion $\chi(\bar{\chi})$ behave as missing energy, and hence the transverse missing energy (\cancel{E}_T) is the natural observable of looking for the signals. Fig. 2(a)

depicts the parton-level Feynman diagrams for the signal, while Fig. 2(b) shows the corresponding irreducible background. The mono- W^\pm production, subsequent to which leptonic decays occur, gives rise to an irreducible background. This background can be effectively mitigated by imposing an appropriate kinematic cut on the transverse mass of the lepton and the transverse missing energy.

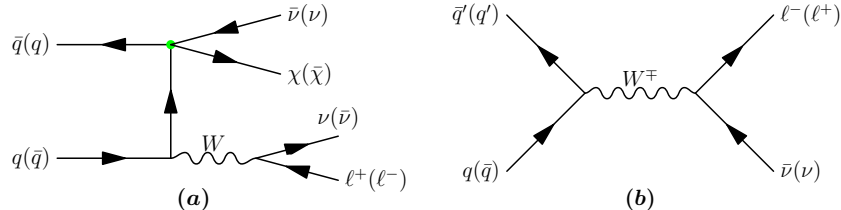


FIG. 2. Feynman diagrams of the mono-lepton process $pp \rightarrow \ell^\pm \cancel{E}_T + X$: (a) is for the signal operators, (b) is for the irreducible background.

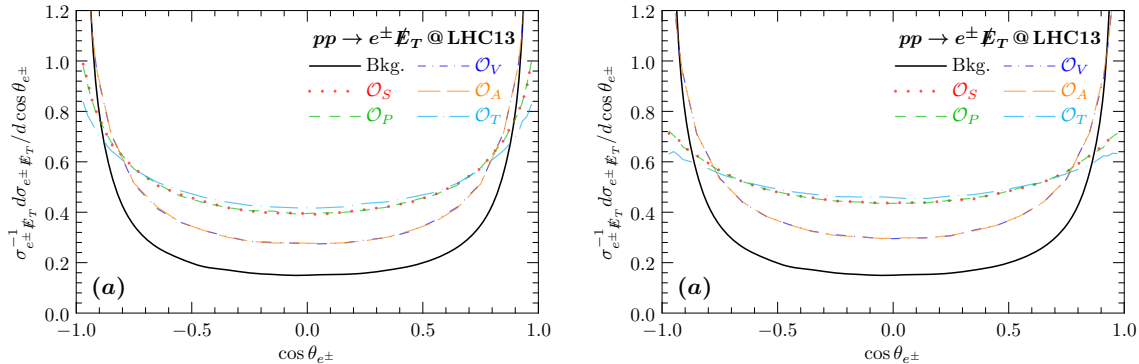


FIG. 3. The parton-level normalized distributions of the polar angle of the outgoing electron (θ_{e^\pm}) are presented for a center-of-mass (CoM) energy of $\sqrt{s} = 13\text{TeV}$. The signal events are depicted by colorful curves. In panel (a), the mass parameter is set to $m_\chi = 0\text{GeV}$, and in panel (b), it is set to $m_\chi = 1\text{TeV}$. The irreducible background is represented by a solid black curve.

Panels (a) and (b) of Fig. 3 exhibit normalized distributions of the polar angle (θ_{e^\pm}). The irreducible background is delineated by a solid-black curve, and the signal events are characterized by colorful non-solid curves. For Fig. 3(a), the model parameters are set as $\Lambda_i = 1\text{TeV}$, $m_\chi = 0\text{GeV}$, while for Fig. 3(b), $m_\chi = 1\text{TeV}$. It is readily apparent that within the central region, the discrepancies in the polar angle distribution are insignificant for differentiating between the signal and the background. This can be predominantly attributed to the fact that W^\pm bosons are emitted along the direction of the incoming partons. In

the forward and backward regions, both the signal events and the irreducible background are conspicuously intense. As shown in Fig. 3(b), the divergence among the signal events induced by the four operators with distinct Lorentz structures becomes more pronounced as m_χ increases. However, in practical scenarios, discerning this divergence may prove to be extremely difficult. The substantial background in these regions has the potential to obscure the unique characteristics of signal operators.

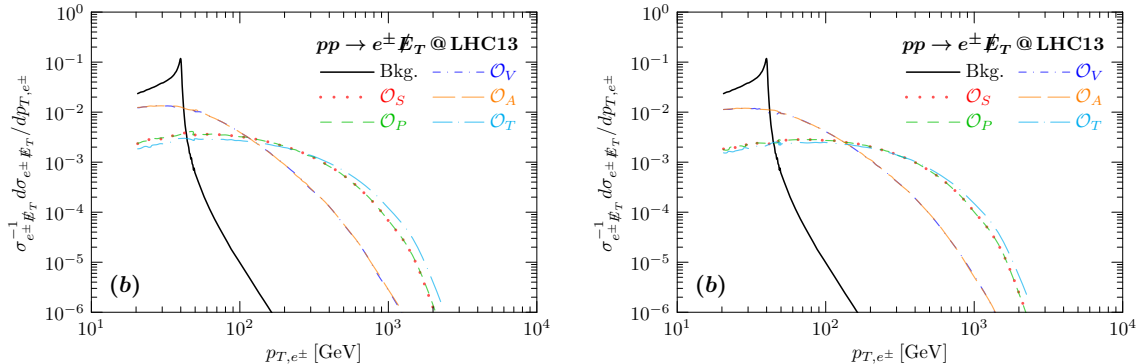


FIG. 4. The normalized parton-level distributions of the transverse momentum of the outgoing electron (p_{T,e^\pm}) are presented for a center-of-mass energy of $\sqrt{s} = 13\text{TeV}$. The signal events are represented by colorful lines. For the panel (a), the signal corresponds to parameters $\Lambda_i = 1\text{TeV}$ and $m_\chi = 0\text{GeV}$, while for the panel (b), the signal is characterized by $\Lambda_i = 1\text{TeV}$ and $m_\chi = 1\text{TeV}$. The irreducible background is depicted by a solid black curve.

The utility of the mono-lepton process is clearly demonstrated by analyzing the transverse momentum distributions in Figs. 4(a) and (b). Charged leptons from W^\pm boson decays typically have a transverse momentum peak at around half the W^\pm boson mass, i.e., $p_{\ell,T} \sim m_W/2$. This characteristic is crucial for analyzing the signal under different conditions: $\Lambda_i = 1\text{TeV}$, $m_\chi = 0\text{GeV}$ in Fig. 4(a) and $m_\chi = 1\text{TeV}$ in Fig. 4(b). In both cases, the transverse momentum distribution of the irreducible background, shown as a black solid curve, has a prominent peak and rapidly declines when (p_T, e^\pm) exceeds the mass threshold. This feature helps distinguish the signal from the background, improving the dark-fermion detection sensitivity via the mono-lepton channel. Moreover, the transverse momentum distributions intuitively show the differences in Lorentz structures between operators. Signals induced by \mathcal{O}_S , \mathcal{O}_P , especially \mathcal{O}_P , dominate the higher (p_T, e^\pm) region. This suggests that the mono-lepton search is highly sensitive to the tensor operator, highlighting its effectiveness

in detecting high-transverse-momentum signals.

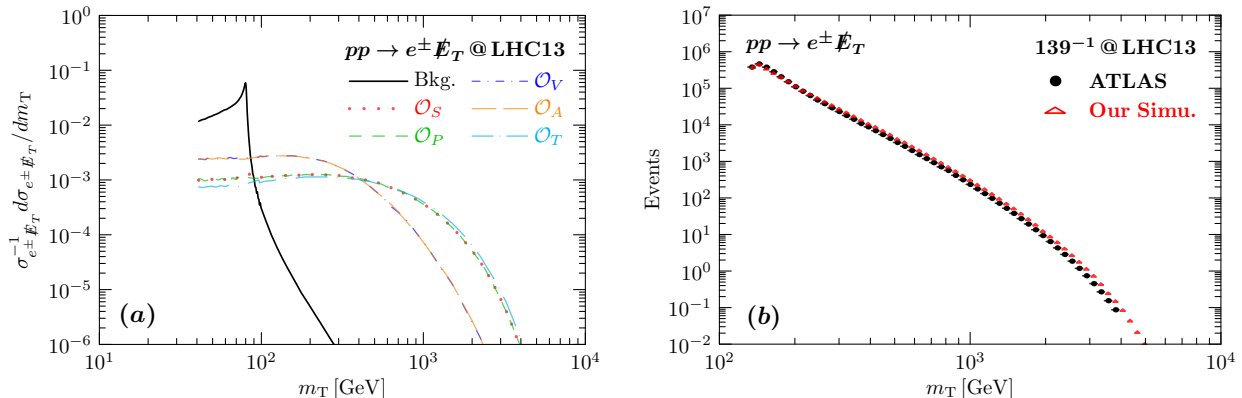


FIG. 5. **Panel (a)**: The normalized parton-level distributions of the transverse mass (m_T) of the outgoing electron are presented for a center-of-mass (CoM) energy of $\sqrt{s} = 13\text{TeV}$. The signal events with $m_\chi = 0\text{GeV}$ and $\Lambda_i = 1\text{TeV}$ are represented by colorful non-solid curves, while the irreducible background is represented by a solid black curve. **Panel (b)**: Validation of our simulation for the transverse mass (m_T) distribution of the irreducible background channel $pp \rightarrow W^\pm \rightarrow e^\pm \nu$ at the LHC is performed with a total luminosity of $\mathcal{L} = 139\text{fb}^{-1}$. The experimental data (black dots) are taken from Ref. [63], and our results (red rectangles) have been renormalized by multiplying an overall constant.

Fig. 5(a) presents the normalized parton-level distribution of the transverse mass. A highly conspicuous peak at $m_T = m_W$ is discernible in the background, which is rigorously defined by the formula:

$$m_T = \sqrt{2p_{\ell,T} \cancel{E}_T (1 - \cos \phi_{\ell\nu})}. \quad (7)$$

In this context, $p_{\ell,T}$ stands for the transverse momentum of the charged lepton, \cancel{E}_T denotes the missing transverse energy, and $\phi_{\ell\nu}$ represents the azimuthal angular separation between the charged lepton and the missing transverse momentum in the transverse plane. The transverse mass stands out as a pivotal parameter for disentangling signal and background events.

Both the ATLAS [64, 65] and CMS [66] collaborations utilize the transverse mass in their meticulous analyses of heavy charged boson production through mono-lepton channels to explore the frontiers of potential new physics. At the parton level, the charged lepton and the missing transverse momentum are consistently anti-aligned in the transverse plane.

As a direct consequence, the transverse mass simplifies to precisely twice the transverse momentum of the charged lepton, i.e., $m_T = 2p_{\ell,T}$. This exact mathematical relationship assumes a preeminent role in experimental analyses at particle colliders, as it empowers researchers to distinguish effectively between signal and background processes.

In Fig. 5(a), the production rate undergoes a precipitous decline beyond the resonant peak of the transverse mass m_T . In contrast, signal distributions exhibit an elongated tail at higher m_T values. This stark disparity in the distribution profiles unequivocally demonstrates that the transverse mass m_T emerges as an outstanding observable for differentiating signal events from background noise in the realm of particle physics experiments.

To validate the simulated distribution of the transverse mass, we conduct a comparison with the ATLAS results, which are derived from a substantially larger luminosity of 139 fb^{-1} . Our event - selection protocol mandates that both the \cancel{E}_T and the $p_{e,T}$ surpass 65GeV . Furthermore, the charged lepton's rapidity is restricted to the range $|\eta_e| < 2.5$, with the barrel - endcap transition regions where $1.37 < |\eta_e| < 1.52$ being excluded. The signal region is precisely demarcated by a transverse mass threshold of $m_T > 130\text{GeV}$. This methodological approach ensures that our simulation undergoes a meticulous benchmarking process against high - luminosity experimental data. The results of this validation are presented in Fig. 5(b). In our analysis, the outcomes are normalized via a universal scale factor, $\epsilon_D = 0.65$, to bring them in line with the total count of irreducible background events documented in the experimental data. This normalization factor primarily serves to account for the effects introduced by the detector. The consistency manifested between our results and the ATLAS data serves to accentuate the efficacy of applying an overall normalization factor. This remarkable congruence validates that the normalization approach not only succeeds in matching the total event counts but also in accurately portraying the differential distributions.

Fig. 6 illustrates the projected exclusion limits at a 95% confidence level (C.L.) within the $m_\chi - A$ parameter space. These exclusion limits relevant to the LHC13 are ascertained via the following χ^2 computation:

$$\chi^2 = \sum_i \left[\frac{\epsilon_D \cdot N_i^S}{\sigma_i^{\text{ATLAS}}} \right]^2, \quad (8)$$

In this context, σ_i^{ATLAS} stands for the experimental uncertainty associated with the i -th bin, as reported by the ATLAS research team, and N_i^S denotes the amount of signal events in

that bin. The factor $\epsilon_D = 0.65$, as previously expounded upon, is utilized to compensate for detector efficiency. This analytical strategy facilitates a stringent comparison and validation against the foreseen experimental outcomes at the LHC. The mono-lepton process demon-

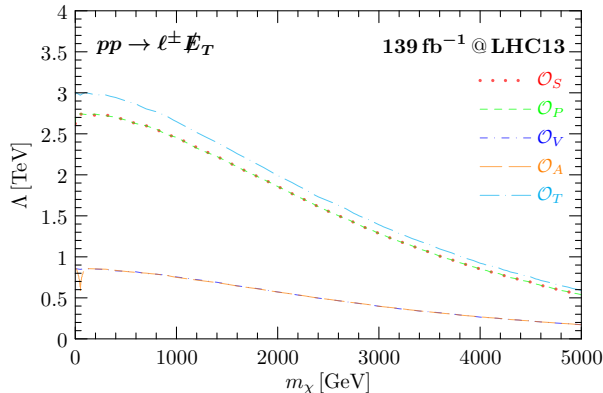


FIG. 6. The expected exclusion limits at a 95% confidence level (C.L.) are presented for the Large Hadron Collider (LHC) operating at a center-of-mass energy of $\sqrt{s} = 13\text{TeV}$ and with a total integrated luminosity of $\mathcal{L} = 139\text{fb}^{-1}$.

strates a pronounced sensitivity to tensor operators. For a massless dark fermion, it can probe up to approximately 3TeV. This elevated sensitivity stems from a larger number of events triggered by tensor operators in the high- m_T region, as shown in Fig. 7. Conversely, the constraints on (axial-)vector operators are relatively weaker. When $m_\chi \approx 0$, the lower detection limit is around 1TeV. Nevertheless, these differences become less significant as the mass of the dark fermion rises.

For the mono-lepton production process driven by four-fermion contact operators, the signal cross-sections increase as the CoM energy rises. In stark contrast, the corresponding background cross-sections decrease as the CoM energy goes up. Given the remarkable improvements in CoM energy and luminosity, the future renditions of the LHC [67] and the Super Proton-Proton Collider (SppC) [68, 69] are excellently positioned to present substantial benefits in the exploration of DM via these operators. The corresponding kinematic cuts for the three production processes are meticulously presented in Tab. I.

Process	14 TeV, 3 ab ⁻¹	25 TeV, 20 ab ⁻¹
$pp \rightarrow e^\pm \cancel{E}_T$	$ \eta_e \leq 2.5$	
	$p_{T,e} \geq 65\text{GeV}$	$p_{T,e} \geq 150\text{GeV}$
	$\cancel{E}_T \geq 65\text{GeV}$	$\cancel{E}_T \geq 150\text{GeV}$

TABLE I. The configurations of the LHC upgrades and the corresponding kinematic cuts at the parton level are presented.

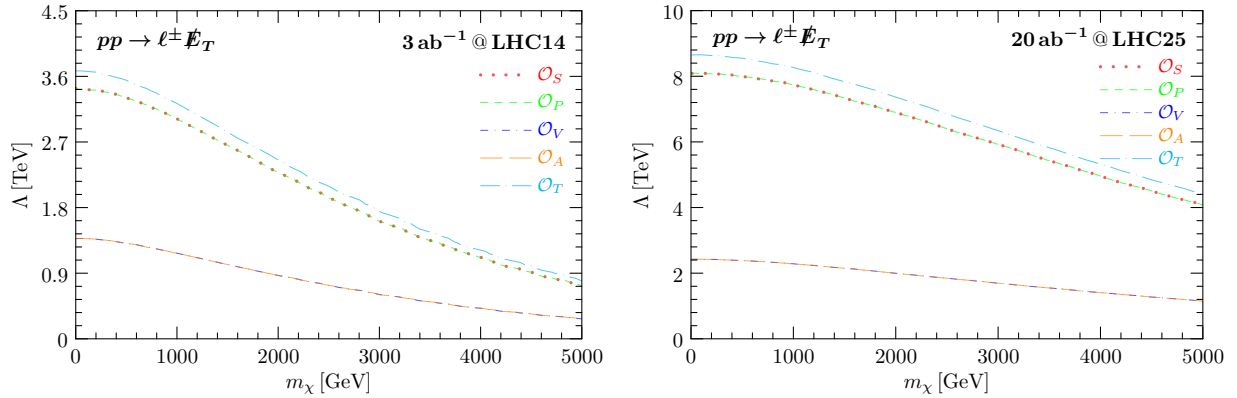


FIG. 7. The expected exclusion limits at a 95% confidence level are shown for the LHC when it operates at a CoM energy of $\sqrt{s} = 13\text{TeV}$ and an integrated luminosity of $\mathcal{L} = 139\text{fb}^{-1}$.

IV. ABSORPTIONS AT NUCLEAR TARGET

Studying non - trivial nucleon - level interactions induced by parton - level operators is a promising approach for direct DM detection. We focus on the inelastic scattering process where a dark fermion is completely converted to a neutrino, and its mass is fully absorbed to form the final nucleus [44, 46]:

$$\chi(p_\chi) + A(p_{in}) \rightarrow \nu(p_\nu) + A(p_{fi}) \quad (9)$$

Here, p_{in} and p_{fi} denote the momenta of the initial and final states, and the mass number A represents the input and output nuclear targets. The differential scattering rate per nuclear recoil energy E_R is given by

$$\frac{dR_A}{dE_R} = N_A n_\chi \int d^3v f_{\mathbf{E}}(\mathbf{v}_\chi, t) v_\chi \frac{d\sigma_A}{dE_R} \quad (10)$$

where N_A is the number of nuclear targets. Usually, the total rate is the sum of individual contributions from each isotope. The local number density of DM is $n_\chi = \rho_\chi/m_\chi$, with a local energy density $\rho_\chi \simeq 0.3 \text{ GeV}/\text{cm}^3$. Moreover, $d\sigma_A/dE_R$ is the differential cross - section of the absorption process in (9), and $f_E(\mathbf{v}_\chi, t)$ is the velocity distribution of the absorbed DM.

In the absorption process, the leading-order recoil energy of the nucleus is approximately proportional to the square of the DM mass m_χ^2 , where m_χ is substantially smaller than the nucleus mass m_A , and this relationship is given by $E_R^0 = m_\chi^2/2(m_A + m_\chi) \approx m_\chi^2/2m_A$. As a result, the differential cross - section peaks sharply at E_R^0 , which can be modeled by the Dirac Delta function:

$$\frac{d\sigma_A}{dE_R} = \frac{|\overline{\mathcal{M}_A}|^2}{16\pi m_A^2 v_\chi} \delta(E_R - E_R^0) \quad (11)$$

Here, \mathcal{M}_A is the helicity amplitude of the process in (9), defined as

$$|\overline{\mathcal{M}_A}|^2 \equiv \frac{1}{2s_\chi + 1} \frac{1}{2J + 1} \sum_{\substack{\text{initial} \\ \text{final spins}}} |\mathcal{M}_A|^2 \quad (12)$$

where J is the total spin of the nucleus and $s_\chi = 1/2$ is the spin of the dark fermion. For non-relativistic DM, the dominant contribution to the scattering amplitude \mathcal{M} occurs when the DM momentum $p_\chi \rightarrow 0$. This indicates that the leading-order amplitude of the absorption process is independent of the DM velocity. Thus, the velocity term in (10) can be treated separately, simplifying the theoretical analysis of DM interactions. The DM velocity distribution function $f_E(\mathbf{v}_\chi, t)$ is normalized to 1, and the differential scattering rate can be rewritten as

$$\frac{dR_A}{dE_R} = \frac{N_A n_\chi}{16\pi m_A^2} |\overline{\mathcal{M}_A}|^2 \delta(E_R - E_R^0) \Theta(E_R - E_R^{\text{th}}) \quad (13)$$

where E_R^{th} is the recoil energy threshold, and the step function $\Theta(E_R - E_R^{\text{th}})$ accounts for the minimum observable energy in an experiment.

For simplicity, this analysis focuses solely on the coherent process. Effective operators with different Lorentz structures can induce both spin-independent (SI) and spin-dependent (SD) interactions, which are differentiated by a coherence factor C_N at the nuclear level. The corresponding differential rate of recoil events can be written as

$$\mathcal{M}_A(q^2) = \sum_{N=p,n} F_{\text{Res}}^N(q^2) \mathcal{M}_{\text{PLN}}^N(q^2) = \sum_{N=p,n} F_{\text{Res}}^N(q^2) C_N \mathcal{M}_N(q^2) \quad (14)$$

where the squared momentum transfer q^2 is defined as $(p_{fi} - p_{in})^2 = (p_\nu - p_\chi)^2$. The amplitude $\mathcal{M}_{\text{PLN}}^N(q^2)$ describes the DM scattering off a point - like nucleus (PLN) and is derived from the amplitude for scattering off a single nucleon, $\mathcal{M}_N(q^2)$, normalized to the nuclear mass m_A . Moreover, $F_{\text{Res}}^N(q^2)$ represents the corresponding nuclear response functions that characterize the nuclear effects on the scattering process at different momentum transfers. The coherence of nucleon spin states differs between SI and SD interactions, influencing the value of the coherence factor C_N . In SI processes, C_N equals Z for protons and $A - Z$ for neutrons. In contrast, for SD interactions, the coherence factor simplifies to $C_N = 1$, indicating a uniform contribution from both protons and neutrons without interference.

A. Spin-Independent Absorption

As illustrated in (14), the SI absorption process at the nuclear scale is directly associated with the nucleon - level amplitude:

$$\mathcal{M}_A = \sum_{N=p,n} F_{SI}^N(q^2) C_N \mathcal{M}_N \quad (15)$$

The SI-specific response function $F_{SI}^N(q^2)$ can typically be characterized by the Helm form factor $F_{\text{Helm}}(q^2)$ of the target nucleus. We follow the formulation detailed in Refs. [70, 71]. Furthermore, when accounting for the conservation of isospin symmetry, which indicates that the disparity between the scattering amplitudes off a proton and a neutron is insignificant, we find that $\mathcal{M}_p = \mathcal{M}_n$.

Based on the non-relativistic expansions in Refs. [13], the scalar and vector components defined in (1) can make substantial contributions to SI absorption; thus, $I = S$ and V . Through simple calculations, we obtain an excellent expression for the squared average of the amplitude:

$$\overline{|\mathcal{M}_N^S|^2} = \frac{4m_A^2 m_\chi^2}{\Lambda_S^4} F_S^N, \quad F_S^N = \sum_q \frac{F_S^{q/N}}{m_q}, \quad (16)$$

$$\overline{|\mathcal{M}_N^V|^2} = \frac{4m_A^2 m_\chi^2}{\Lambda_V^4} F_V^N, \quad F_V^N = \sum_q F_1^{q/N}, \quad (17)$$

Assuming that the DM couples universally to quarks, we gather all relevant terms to deter-

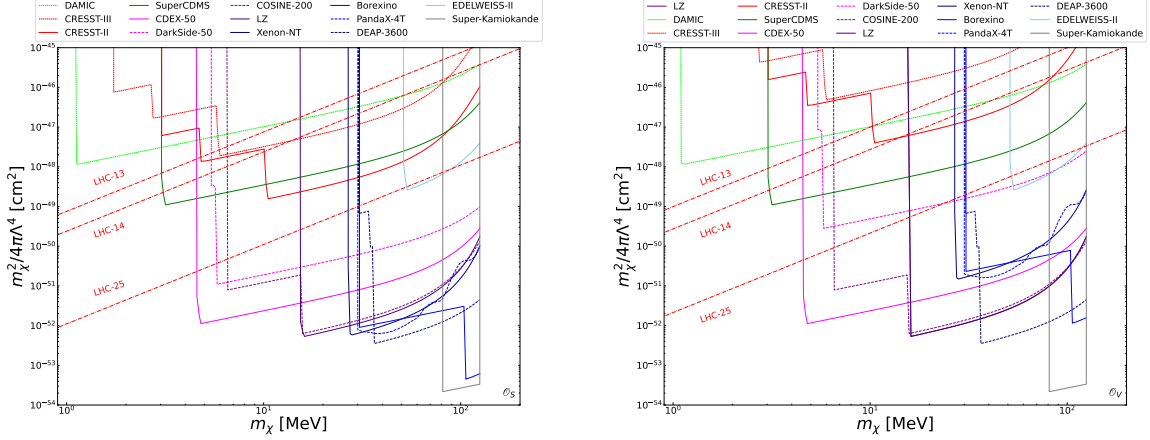


FIG. 8. Excluded regions in the $m_\chi^2/4\pi\Lambda^4 - m_\chi$ plane for the scalar (*left panel*) and vector (*right panel*) operators.

mine the scattering rate as follows:

$$R_A^\Gamma = N_A n_\chi \frac{m_\chi^2}{4\pi\Lambda_\Gamma} [AF_\Gamma^N(m_\chi^2)F_{\text{Helm}}(m_\chi^2)]^2 \Theta(E_R^0 - E_R^{\text{th}}), \quad (18)$$

where we use the approximation $q^2 \approx m_\chi^2$. The excluded regions obtained in the $m_\chi^2/4\pi\Lambda^4 - m_\chi$ plane for \mathcal{O}_S and \mathcal{O}_V are presented in Fig. 8. Evidently, the Super-Kamiokande collaboration imposes the strongest constraint on the SI scattering cross section for fermionic DM due to its large exposure. Moreover, compared with the LHC bounds, the absorption process always provides stronger constraints in the region $m_\chi \in [\sim 10, \sim 100]$ MeV. We will explore the other experiments listed in Tab. III.

However, the high recoil energy threshold in Super-Kamiokande implies that it will only enforce strong constraints for heavy DM. Given that lighter nuclei are highly efficient in probing light DM candidates, we can project the scattering outcomes off individual hydrogen nuclei in future experiments within the mass range $m_\chi \in [\sim 0, \sim 1]$ MeV. This projection assumes an energy threshold E_{th} of 1 eV and an exposure of 100 kg.yr [44], as depicted in Fig. 9 for \mathcal{O}_S and \mathcal{O}_T . Evidently, the LHC imposes the most stringent direct constraints, highlighting the collider's effectiveness as a potent tool for detecting light DM.

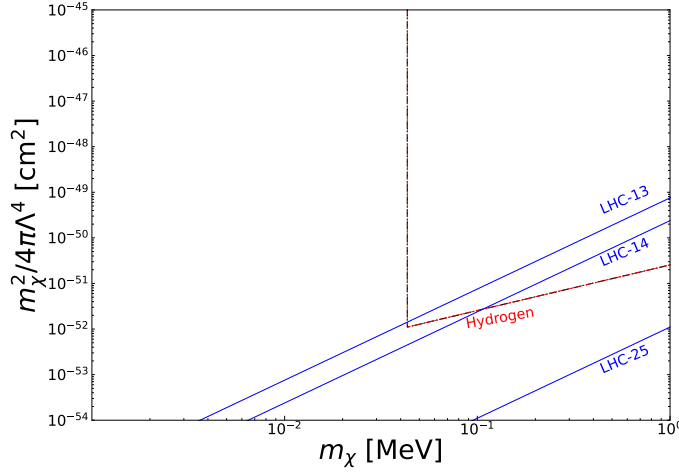


FIG. 9. Excluded regions in the $m_\chi^2/4\pi\Lambda^4 - m_\chi$ plane for scalar and vector operators when considering hydrogen as the target nuclei.

B. Spin-Dependent Absorption

The SD interactions can be triggered by pseudo-scalar and axial-vector operators. Generally, the leading order contribution of the pseudo-scalar operator is suppressed by an additional factor of $q/m_A \sim m_\chi/m_A$. The leading order nonrelativistic nucleon matrix elements for the pseudo-scalar and axial-vector operators can be written as follows:

$$\mathcal{O}_P^N = 2\sqrt{2}h_\nu m_\chi F_P^N [(\xi_{h_\nu}^\nu)^\dagger \xi_{h_\chi}^\chi] [(\omega_{h_{N'}}^{N'})^\dagger (\mathbf{q} \cdot \mathbf{s}) \omega_{h_N}^N], \quad (19)$$

$$\mathcal{O}_A^N = 8\sqrt{2}m_\chi m_A F_A^N [(\xi_{h_\nu}^\nu)^\dagger \mathbf{s} \xi_{h_\chi}^\chi] [(\omega_{h_{N'}}^{N'})^\dagger \mathbf{s} \omega_{h_N}^N], \quad (20)$$

Given that the amplitude can be represented as the coherent sum of individual nucleon contributions, the corresponding total amplitude is as follows:

$$\mathcal{M}_A^A = \sum_{N=p,n} \mathbf{s}_\chi \cdot \langle J, M' | \mathbf{S}_N | J, M \rangle, \quad (21)$$

$$\mathcal{M}_P^A = \sum_{N=p,n} \mathbb{I}_\chi [\langle J, M' | \mathbf{S}_N | J, M \rangle \cdot \mathbf{q}], \quad (22)$$

Here, \mathbf{s}_χ represents the spin operators of the DM or neutrino, and \mathbb{I}_χ is the identity operator of this spinor space. For a nuclear state with total spin J and helicity M , \mathbf{S}_N denotes the total nucleon spin operator, where $\mathbf{S}_p \equiv \sum_{i=\text{protons}} \mathbf{s}_{p_i}$ and $\mathbf{S}_n \equiv \sum_{i=\text{neutrons}} \mathbf{s}_{n_i}$ for protons and neutrons, respectively. In a spinless nuclear state, where the total spin $J = 0$,

the above matrix elements clearly become zero. Tab. III lists some typical experiments involving isotopes with non-zero total spin. These experiments effectively impose excellent constraints on the SD scattering cross section for fermionic DM in this study.

Upon summing over the final state spins and averaging over the initial states, the squared amplitudes are provided as follows:

$$\overline{|\mathcal{M}_A^A|^2} = \frac{1}{2} \sum_{N,N'} F_{4,4}^{NN'} = \sum_{N,N'} \frac{1}{32} \left[F_{\Sigma'}^{NN'}(q^2) + F_{\Sigma''}^{NN'}(q^2) \right], \quad (23)$$

$$\overline{|\mathcal{M}_P^A|^2} = \sum_{N,N'} F_{10,10}^{NN'} = \sum_{N,N'} \frac{q^2}{4} F_{\Sigma''}^{NN'}(q^2), \quad (24)$$

Here, the additional factor of 1/2 is attributed to the fact that only left-handed neutrinos partake in the scattering.

The explicit expressions of $F_{\Sigma'}^{NN'}(q^2)$ and $F_{\Sigma''}^{NN'}(q^2)$ are defined in Ref. [72]. The approximation of zero momentum transfer can be concisely written as:

$$\sum_{M,M'} \langle J, M | S_{N',i} | J, M' \rangle \langle J, M' | S_{N,j} | J, M \rangle = \frac{(J+1)(2J+1)}{3J} \mathbb{S}_N \mathbb{S}_{N'} \delta_{ij} \quad (25)$$

Here, $\mathbb{S}_N \equiv \langle J, J | S_N^z | J, J \rangle$ denotes the expectation values of the nuclear spin operator for states with maximal angular momentum. The response functions involving \mathbb{S}_N are then given as:

$$F_{4,4}^{NN'} = \frac{J+1}{4J} \mathbb{S}_N \mathbb{S}_{N'}, \quad F_{\Sigma'}^{NN'} + F_{\Sigma''}^{NN'} = \frac{4(J+1)}{J} \mathbb{S}_N \mathbb{S}_{N'}, \quad (26)$$

$$F_{10,10}^{NN'} = \frac{J+1}{3J} q^2 \mathbb{S}_N \mathbb{S}_{N'}, \quad F_{\Sigma''}^{NN'} = \frac{4(J+1)}{3J} \mathbb{S}_N \mathbb{S}_{N'}. \quad (27)$$

The q^2 dependence of the response function $F_{10,10}^{NN'}$ can be factored out using the approximation $F_{10,10}^{NN'}(q^2 = 0) = \frac{q^2}{4} F_{\Sigma''}^{NN'}(q^2 = 0)$. Moreover, the model - dependent parameter \mathbb{S}_N is determined via detailed calculations within realistic nuclear models. We list the values of \mathbb{S}_N in Tab. IV. For more details on \mathbb{S}_N , we direct the reader to Ref. [73].

In our study, when calculating the scattering rate, we assume that either a proton or a neutron takes part in the interaction. Additionally, only the nucleon with the largest spin expectation value contributes to the scattering rate. After accounting for the phase space factor, the scattering rate is then given by:

$$R_A^P = \frac{N_A n_\chi m_\chi^4}{8\pi \Lambda_P^4 m_A^2} \Theta(E_R^0 - E_R^{\text{th}}) \sum_{N,N'=p,n} F_P^N F_P^{N'} [F_{\Sigma''}^{NN'}], \quad (28)$$

$$R_A^A = \frac{N_A n_\chi m_\chi^2}{4\pi\Lambda_A^4} \Theta(E_R^0 - E_R^{\text{th}}) \sum_{N, N'=p, n} F_A^N F_A^{N'} [F_{\Sigma'}^{NN'} + F_{\Sigma''}^{NN'}]. \quad (29)$$

Figure 10 shows the excluded regions from SD scatterings in the $m_\chi^2/4\pi\Lambda^4 - m_\chi$ plane for the experiments listed in Tab. III. In nontrivial nucleon level interactions, the constraints

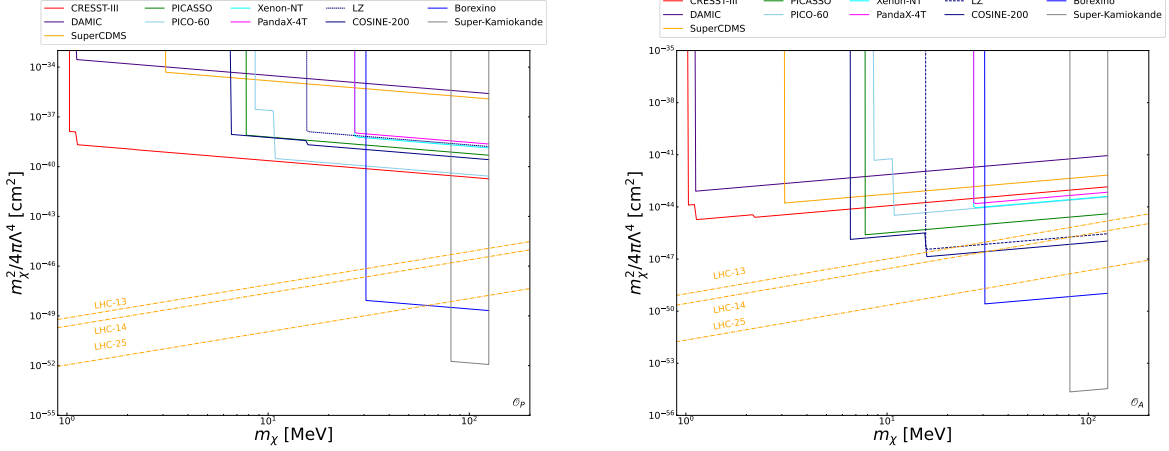


FIG. 10. Excluded regions in the $m_\chi^2/4\pi\Lambda^4 - m_\chi$ plane from SD scatterings for the pseudo - scalar (left) and axial - vector (right) operators.

from the pseudo-scalar operator \mathcal{O}_P are far less stringent than those from the axial-vector operator \mathcal{O}_A . Notably, the Super-Kamiokande collaboration still imposes the tightest constraints compared to other direct detection experiments. The reasons can be summarized as follows: Firstly, (28) shows that the scattering rate of \mathcal{O}_P is suppressed by a factor of m_χ^2/m_A^2 . Thus, the scattering rate of \mathcal{O}_A is significantly larger than that of \mathcal{O}_P . Secondly, the constraints from SD experiments using heavier nuclei are much weaker than those using lighter nuclear targets. This difference is clearly shown in the results of the Borexino and Super-Kamiokande experiments. These experiments not only have larger exposures but also use lighter isotopes, as detailed in Tab. III. These features greatly enhance the experiments' sensitivity to SD interactions. As a result, the constraints from the Borexino and Super-Kamiokande experiments are stronger than those of most experiments and the LHC bounds.

We also provide constraints from hydrogen targets for the operators \mathcal{O}_P and \mathcal{O}_A in the mass range where $m_\chi \lesssim 1$ MeV. As shown in Fig. 11, the LHC has a clear advantage in the low mass region when compared to direct detection experiments.

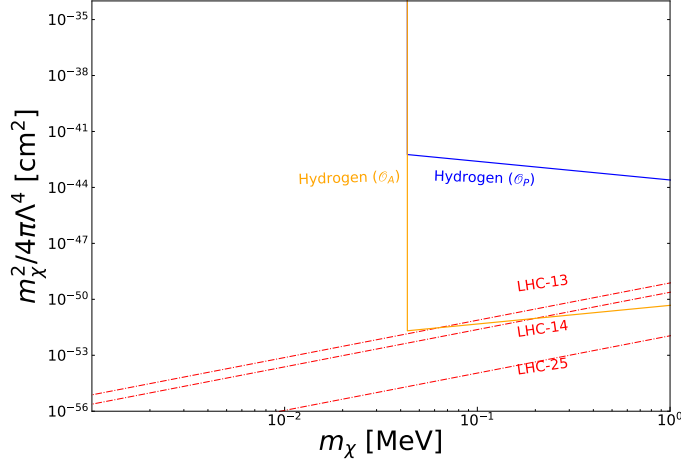


FIG. 11. Excluded regions in the $m_\chi^2/4\pi\Lambda^4$ - m_χ plane due to SD scatterings for the pseudo-scalar and axial-vector operators with hydrogen as the target.

C. Absorption for the Tensor Operator

The quark level tensor operator \mathcal{O}_T can induce both SI and SD interactions at the nucleon level. Therefore, the total interaction amplitude is the combined sum of these two contributions:

$$\mathcal{M}_{A,T} = \mathcal{M}_{A,T}^{SD} + \mathcal{M}_{A,T}^{SI}. \quad (30)$$

Similar to the SD absorption case in (21), the scattering amplitude for the tensor operator can be expressed as:

$$\mathcal{M}_{A,T}^{SD} = 16\sqrt{2}m_\chi m_A \sum_{N=p,n} F_{T,SD}^N [\mathbf{s}_\chi \cdot \langle J, M' | \mathbf{S}_N | J, M \rangle], \quad F_{T,SD}^N = \sum_q \frac{F_{T,0}^{q/N}}{m_q}. \quad (31)$$

For the SI interaction, the corresponding scattering amplitude is:

$$\mathcal{M}_{A,T}^{SI} = 4\sqrt{2}m_\chi \sum_{N=p,n} F_{T,SI}^N C_N F_{SI}^N [\mathbf{s}_\chi \cdot \mathbf{q}] \delta_{M'M}, \quad F_{T,SI}^N = \sum_q \frac{F_{T,1}^{q/N} + 2F_{T,2}^{q/N}}{m_q}. \quad (32)$$

Therefore, the total average squared amplitude is given by:

$$\overline{|\mathcal{M}_{T,L}|^2} = \overline{|\mathcal{M}_{T,SD}|^2} + \overline{|\mathcal{M}_{T,SI}|^2} + \overline{\mathcal{M}_{T,SD}^\dagger \mathcal{M}_{T,SI} + \mathcal{M}_{T,SI}^\dagger \mathcal{M}_{T,SD}}. \quad (33)$$

After summing over the helicity states of both DM particles and neutrinos, the interference term can be reformulated as follows:

$$\Re\{\overline{\mathcal{M}_{T,SD}^\dagger \mathcal{M}_{T,SI}}\} \propto \sum_M \langle J, M | \mathbf{q} \cdot \mathbf{S}_N | J, M \rangle. \quad (34)$$

However, since the nuclear target is always unpolarized and the orientation of momentum transfer is isotropic, the interference term makes a negligible contribution to the total event rate. This is because the overall scattering rate represents an incoherent sum of the SD and SI contributions:

$$R_A^T = R_{A,SD}^T + R_{A,SI}^T, \quad (35)$$

where the detailed expressions for the SD and SI scattering rates are as follows:

$$R_{A,SD}^T = \frac{16N_A n_\chi m_\chi^2}{\pi \Lambda_T^4} \Theta(E_R^0 - E_R^{\text{th}}) \sum_{N,N'=p,n} F_{T,SD}^N F_{T,SD}^{N'} [F_{\Sigma'}^{NN'} + F_{\Sigma''}^{NN'}], \quad (36)$$

$$R_{A,SI}^T = N_A n_\chi \frac{m_\chi^4}{4\pi \Lambda_T m_A^2} [A F_{T,SI}^N F_{\text{Helm}}(m_\chi^2)]^2 \Theta(E_R^0 - E_R^{\text{th}}). \quad (37)$$

From (36), it is evident that the SI contribution is suppressed by a factor of m_χ^2/m_A^2 , similar to the pseudo-scalar contribution to the SD scattering discussed in the previous section. The left panel of the Fig. 12 shows the excluded regions in the $m_\chi^2/4\pi\Lambda^4 - m_\chi$ plane due to SD scatterings for the tensor operator. Clearly, the Borexino and Super-Kamiokande experiments are still the most promising methods for detecting the absorption signal. Moreover, the constraints imposed by the LHC cover nearly all those derived from direct detection experiments and are particularly dominant in the low DM mass region. This superiority is clearly shown in the right panel of the Fig. 12.

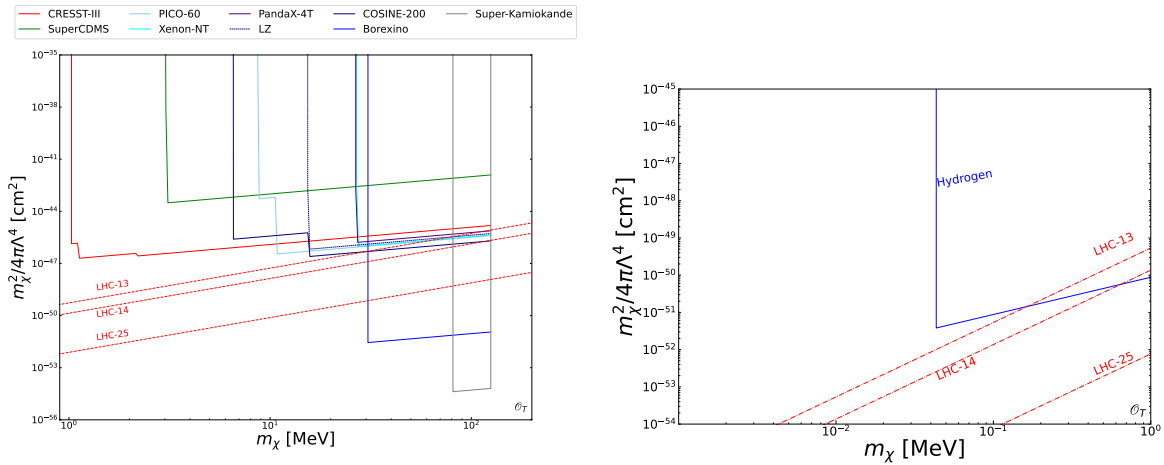


FIG. 12. Excluded regions in the $m_\chi^2/4\pi\Lambda^4 - m_\chi$ plane due to SD scatterings for the tensor operator. The **left panel** represents the heavy target, while the **right panel** is for the hydrogen target.

V. CONCLUSION

In this paper, we investigate four-fermion contact operators that involve a dark fermion, a neutral neutrino, and a quark pair. We assess the sensitivity of these operators at the LHC through mono-lepton production processes. To validate our results, we compare the simulated distributions with the data from the ATLAS experiment. We also emphasize the substantial potential of future upgrades to the LHC for exploring fermionic DM. Moreover, we contrast the constraints from DM direct detection experiments with those obtained from LHC measurements. This comparison reveals the LHC's distinct advantage in probing light DM ($m_\chi \in [\sim 0, \sim 1] \text{ MeV}$) and at the TeV scale.

Nevertheless, direct detection experiments, such as Super-Kamiokande and Borexino, still provide competitive constraints. These experiments benefit from the use of sufficiently light nuclei and large exposure, along with a unique recoil energy spectrum. In addition, for the operators \mathcal{O}_S and \mathcal{O}_V , SI scattering with heavy nuclear targets shows well defined exclusion regions. In contrast, SD scattering for the operators \mathcal{O}_P , \mathcal{O}_A , and \mathcal{O}_T exhibits more stringent constraints.

Appendix A: Experimental Parameters for SI and SD Absorption

The Tab. II presents the experiments analyzed in this paper for probing the SI absorption signal. Additionally, some typical experiments, which include isotopes with non-zero total spin, are listed in Tab. III. Furthermore, we list the spin expectation value S_N of some isotopes that will be studied in this paper.

ACKNOWLEDGMENTS

K.M. was supported by the Natural Science Basic Research Program of Shaanxi (Program No. 2023-JC-YB-041).

[1] J.F. Navarro, C.S. Frenk and S.D.M. White, *The Structure of cold dark matter halos*, *Astrophys. J.* **462** (1996) 563 [[astro-ph/9508025](#)].

Experiment	Target	Exposure	E_R^{th}
Super-Kamiokande [74]	H ₂ O	171000 t yr	3.5 MeV
CRESST-II [75]	CaWO ₄	52 kg day	307 eV
CRESST-III [76]	CaWO ₄	2.39 kg day	100 eV
DarkSide-50 [77, 78]	Liquid Ar	6787 kg day	0.6 keV
XENONnT [79]	Liquid Xe	1.09 t yr	3 keV
PandaX-4T [80]	Liquid Xe	0.55 t yr	3 keV
Borexino [81]	C ₆ H ₃ (CH ₃) ₃	958.58 t yr	500 keV
PICO-60 [82]	CF ₃ I	3415 kg day	20 keV
EDELWEISS-II [83]	Ge	384 kg day	20 keV
COSINE-200 [84]	NaI	0.6 t yr	1 keV
LZ [85]	Liquid Xe	0.9 t yr	1 keV
SuperCDMS [86]	Ge	36.9 kg day	70 eV
DAMIC [87]	Si	3.25 kg day	23 eV
DEAP-3600 [88]	Liquid Ar	7.35 t yr	17.5 keV
CDEX-50 [89]	Ge	150 jg yr	160 eV

TABLE II. *Experiments studied here for probing the SI absorption signals.*

- [2] D. Clowe, M. Bradac, A.H. Gonzalez, M. Markevitch, S.W. Randall, C. Jones et al., *A direct empirical proof of the existence of dark matter*, *Astrophys. J. Lett.* **648** (2006) L109 [[astro-ph/0608407](#)].
- [3] D.N. Spergel and P.J. Steinhardt, *Observational evidence for selfinteracting cold dark matter*, *Phys. Rev. Lett.* **84** (2000) 3760 [[astro-ph/9909386](#)].

Experiment	Target	Exposure	Isotope (Abund.)	E_R^{th}
Super-Kamiokande [74]	H ₂ O	171000 t yr	^1_1H (99.985%)	3.5 MeV
XENONnT [79]	Liquid Xe	1.09 t yr	$^{129}_{54}\text{Xe}$ (26.4%) $^{131}_{54}\text{Xe}$ (21.2%)	3 keV
PandaX-4T [90]	Liquid Xe	0.63 t yr	$^{129}_{54}\text{Xe}$ (26.4%) $^{131}_{54}\text{Xe}$ (21.2%)	3 keV
Borexino [81]	C ₆ H ₃ (CH ₃) ₃	817 t yr	$^{13}_6\text{C}$ (1.1%) ^1_1H (99.985%)	500 keV
CRESST-III [91]	LiAlO ₂	2.345 kg day	^6_3Li (7.5%) ^7_3Li (92.5%) $^{27}_{13}\text{Al}$ (100%)	94.1 eV
PICO-60 [82]	CF ₃ I	2207 kg day	$^{13}_6\text{C}$ (1.1%) $^{19}_9\text{F}$ (100%)	3.3 keV
PICASSO [92]	F	114 kg day	$^{19}_9\text{F}$ (100%)	1.7 keV
COSINE-200 [84]	NaI	0.6 t yr	$^{23}_{11}\text{Na}$ (100%) $^{127}_{53}\text{I}$ (100%)	1 keV
LZ [85]	Liquid Xe	0.9 t yr	$^{129}_{54}\text{Xe}$ (26.4%) $^{131}_{54}\text{Xe}$ (21.2%)	1 keV
SuperCDMS [86]	Ge	36.9 kg day	$^{73}_{22}\text{Ge}$ (27.31%)	70 eV
DAMIC [87]	Si	3.25 kg day	$^{29}_{14}\text{Si}$ (4.7%)	23 eV

TABLE III. *Experiments studied here for probing the SD absorption signals.*

[4] G. Bertone, D. Hooper and J. Silk, *Particle dark matter: Evidence, candidates and constraints*, *Phys. Rept.* **405** (2005) 279 [hep-ph/0404175].

Isotope (Abund.)	J	\mathbb{S}_p	\mathbb{S}_n	Ref.
^1_1H (99.985%)	1/2	0.5	0	[93]
^6_3Li (7.5%)	1/2	0.472	0.472	[91, 94]
^7_3Li (92.5%)	3/2	0.497	0.004	[95]
$^{13}_6\text{C}$ (1.1%)	1/2	-0.009	-0.172	[96]
$^{27}_{13}\text{Al}$ (100%)	5/2	0.343	0.0296	[97]
$^{73}_{22}\text{Ge}$ (27.31%)	9/2	0.37	0.123	[73]
$^{23}_{11}\text{Na}$ (100%)	3/2	-0.051	-0.051	[73]
$^{29}_{14}\text{Si}$ (4.7%)	1/2	-0.009	-0.172	[73]
$^{19}_9\text{F}$ (100%)	1/2	0.339	0.161	[98]
$^{127}_{53}\text{I}$ (100%)	5/2	0.265	0.235	[73]
$^{129}_{54}\text{Xe}$ (26.4%)	1/2	0.0128	0.300	[99]
$^{131}_{54}\text{Xe}$ (21.2%)	3/2	-0.012	-0.217	

TABLE IV. Spin expectation values (\mathbb{S}_N) of the isotopes studied in this paper.

- [5] A. Boveia and C. Doglioni, *Dark Matter Searches at Colliders*, *Ann. Rev. Nucl. Part. Sci.* **68** (2018) 429 [1810.12238].
- [6] G. Arcadi, M. Lindner, Y. Mambrini, M. Pierre and F.S. Queiroz, *GUT Models at Current and Future Hadron Colliders and Implications to Dark Matter Searches*, *Phys. Lett. B* **771** (2017) 508 [1704.02328].
- [7] G. Landsberg, *Moving Beyond Effective Field Theory in Dark Matter Searches at Colliders*, in *50th Rencontres de Moriond on QCD and High Energy Interactions*, pp. 211–216, 6, 2015 [1506.00660].
- [8] G. Steigman, B. Dasgupta and J.F. Beacom, *Precise Relic WIMP Abundance and its Impact on Searches for Dark Matter Annihilation*, *Phys. Rev. D* **86** (2012) 023506 [1204.3622].

- [9] J. de Dios Zornoza, *Review on Indirect Dark Matter Searches with Neutrino Telescopes*, *Universe* **7** (2021) 415.
- [10] C. Pérez de los Heros, *Status, Challenges and Directions in Indirect Dark Matter Searches*, *Symmetry* **12** (2020) 1648 [2008.11561].
- [11] P. Cox, M.J. Dolan and J. Wood, *Absorption of Fermionic Dark Matter via the Scalar Portal*, **2308.00309**.
- [12] S.-F. Ge and O. Titov, *Incoherent Fermionic Dark Matter Absorption with Nucleon Fermi Motion*, **2405.05728**.
- [13] K. Ma, S.-F. Ge, L.-Y. He and N. Zhou, *Complementary Search of Fermionic Absorption Operators at Hadron Collider and Direct Detection Experiments*, **2405.16878**.
- [14] K. Ma, *Exploring Four Fermion Contact Couplings of a Dark Fermion and an Electron at Hadron Colliders and Direct Detection Experiments*, **2404.06419**.
- [15] Y. Hochberg, T. Lin and K.M. Zurek, *Absorption of light dark matter in semiconductors*, *Phys. Rev. D* **95** (2017) 023013 [1608.01994].
- [16] Y. Hochberg, T. Lin and K.M. Zurek, *Detecting Ultralight Bosonic Dark Matter via Absorption in Superconductors*, *Phys. Rev. D* **94** (2016) 015019 [1604.06800].
- [17] A. Mitridate, K. Pardo, T. Trickle and K.M. Zurek, *Effective field theory for dark matter absorption on single phonons*, *Phys. Rev. D* **109** (2024) 015010 [2308.06314].
- [18] S.-F. Ge, X.-G. He, X.-D. Ma and J. Sheng, *Revisiting the fermionic dark matter absorption on electron target*, *JHEP* **05** (2022) 191 [2201.11497].
- [19] PANDAX collaboration, *Search for Light Fermionic Dark Matter Absorption on Electrons in PandaX-4T*, *Phys. Rev. Lett.* **129** (2022) 161804 [2206.02339].
- [20] CDEX collaboration, *First Search for Light Fermionic Dark Matter Absorption on Electrons Using Germanium Detector in CDEX-10 Experiment*, **2404.09793**.
- [21] J.A. Dror, G. Elor, R. McGehee and T.-T. Yu, *Absorption of sub-MeV fermionic dark matter by electron targets*, *Phys. Rev. D* **103** (2021) 035001 [2011.01940].
- [22] S.-F. Ge, K. Ma, X.-D. Ma and J. Sheng, *Associated production of neutrino and dark fermion at future lepton colliders*, *JHEP* **11** (2023) 190 [2306.00657].
- [23] Y. Bai and T.M.P. Tait, *Searches with Mono-Leptons*, *Phys. Lett. B* **723** (2013) 384 [1208.4361].

- [24] CMS collaboration, *Search for dark matter in the mono-lepton channel with pp collision events at center-of-mass energy of 8 TeV*, .
- [25] S. Matsumoto, S. Shirai and M. Takeuchi, *Indirect Probe of Electroweak-Interacting Particles with Mono-Lepton Signatures at Hadron Colliders*, *JHEP* **03** (2019) 076 [[1810.12234](#)].
- [26] H. Dreiner, D. Schmeier and J. Tattersall, *Contact Interactions Probe Effective Dark Matter Models at the LHC*, *EPL* **102** (2013) 51001 [[1303.3348](#)].
- [27] F. Bishara, J. Brod, B. Grinstein and J. Zupan, *From quarks to nucleons in dark matter direct detection*, *JHEP* **11** (2017) 059 [[1707.06998](#)].
- [28] A. Belyaev, E. Bertuzzo, C. Caniu Barros, O. Eboli, G. Grilli Di Cortona, F. Iocco et al., *Interplay of the LHC and non-LHC Dark Matter searches in the Effective Field Theory approach*, *Phys. Rev. D* **99** (2019) 015006 [[1807.03817](#)].
- [29] K. Ma and L.-Y. He, *Constraining Gluonic Contact Interaction of a Neutrino-philic Dark Fermion at Hadron Colliders and Direct Detection Experiments*, [2405.20890](#).
- [30] W. Abdallah, J. Fiaschi, S. Khalil and S. Moretti, *Mono-jet, -photon and -Z signals of a supersymmetric (B – L) model at the Large Hadron Collider*, *JHEP* **02** (2016) 157 [[1510.06475](#)].
- [31] Y. Bai, J. Bourbeau and T. Lin, *Dark matter searches with a mono-Z' jet*, *JHEP* **06** (2015) 205 [[1504.01395](#)].
- [32] G.G. da Silveira and M.S. Mateus, *Investigation of spin-dependent dark matter in mono-photon production at high-energy colliders*, [2308.03680](#).
- [33] J. Kalinowski, W. Kotlarski, K. Mekala, A.F. Zarnecki and K. Zembaczynski, *New approach to DM searches with mono-photon signature*, *PoS ICHEP2022* (2022) 294.
- [34] Y. Gershtein, F. Petriello, S. Quackenbush and K.M. Zurek, *Discovering hidden sectors with mono-photon Z' searches*, *Phys. Rev. D* **78** (2008) 095002 [[0809.2849](#)].
- [35] A.M.H. H., E.-s.A. El-dahshan and S. Elgammal, *Investigating a new neutral heavy gauge boson within the mono-Z' model via simulated pp collisions at $\sqrt{s} = 14$ TeV at the HL-LHC*, [2406.19004](#).
- [36] G. Benítez-Irarrázabal and A.R. Zerwekh, *Mono-Higgs and Mono-Z Production in the Minimal Vector Dark Matter Model*, *Universe* **10** (2024) 288 [[2401.03954](#)].
- [37] S. Kundu, A. Guha, P.K. Das and P.S.B. Dev, *EFT analysis of leptophilic dark matter at future electron-positron colliders in the mono-photon and mono-Z channels*, *Phys. Rev. D*

- 107** (2023) 015003 [[2110.06903](#)].
- [38] N. Wan, N. Li, B. Zhang, H. Yang, M.-F. Zhao, M. Song et al., *Searches for Dark Matter via Mono-W Production in Inert Doublet Model at the LHC*, *Commun. Theor. Phys.* **69** (2018) 617.
- [39] N.F. Bell, Y. Cai and R.K. Leane, *Mono-W Dark Matter Signals at the LHC: Simplified Model Analysis*, *JCAP* **01** (2016) 051 [[1512.00476](#)].
- [40] CMS collaboration, *Search for Dark Matter with mono-X Signatures in CMS*, *PoS TAUP2023* (2024) 074.
- [41] S. Bhattacharya, P. Ghosh, J. Lahiri and B. Mukhopadhyaya, *Mono-X signal and two component dark matter: new distinction criteria*, [2211.10749](#).
- [42] E. Bernreuther, J. Horak, T. Plehn and A. Butter, *Actual Physics behind Mono-X*, *SciPost Phys.* **5** (2018) 034 [[1805.11637](#)].
- [43] PANDAX collaboration, *First Search for the Absorption of Fermionic Dark Matter with the PandaX-4T Experiment*, *Phys. Rev. Lett.* **129** (2022) 161803 [[2205.15771](#)].
- [44] J.A. Dror, G. Elor and R. McGehee, *Absorption of Fermionic Dark Matter by Nuclear Targets*, *JHEP* **02** (2020) 134 [[1908.10861](#)].
- [45] T. Li, J. Liao and R.-J. Zhang, *Dark magnetic dipole property in fermionic absorption by nucleus and electrons*, *JHEP* **05** (2022) 071 [[2201.11905](#)].
- [46] J.A. Dror, G. Elor and R. McGehee, *Directly Detecting Signals from Absorption of Fermionic Dark Matter*, *Phys. Rev. Lett.* **124** (2020) 18 [[1905.12635](#)].
- [47] B. Belfatto, D. Buttazzo, C. Gross, P. Panci, A. Strumia, N. Vignaroli et al., *Dark Matter abundance via thermal decays and leptoquark mediators*, *JHEP* **06** (2022) 084 [[2111.14808](#)].
- [48] G. Busoni, A. De Simone, E. Morgante and A. Riotto, *On the Validity of the Effective Field Theory for Dark Matter Searches at the LHC*, *Phys. Lett. B* **728** (2014) 412 [[1307.2253](#)].
- [49] G. Busoni, A. De Simone, J. Gramling, E. Morgante and A. Riotto, *On the Validity of the Effective Field Theory for Dark Matter Searches at the LHC, Part II: Complete Analysis for the s-channel*, *JCAP* **06** (2014) 060 [[1402.1275](#)].
- [50] G. Busoni, A. De Simone, T. Jacques, E. Morgante and A. Riotto, *On the Validity of the Effective Field Theory for Dark Matter Searches at the LHC Part III: Analysis for the t-channel*, *JCAP* **09** (2014) 022 [[1405.3101](#)].

- [51] R.J. Hill and M.P. Solon, *Universal behavior in the scattering of heavy, weakly interacting dark matter on nuclear targets*, *Phys. Lett. B* **707** (2012) 539 [[1111.0016](#)].
- [52] M.T. Frandsen, U. Haisch, F. Kahlhoefer, P. Mertsch and K. Schmidt-Hoberg, *Loop-induced dark matter direct detection signals from gamma-ray lines*, *JCAP* **10** (2012) 033 [[1207.3971](#)].
- [53] L. Vecchi, *WIMPs and Un-Naturalness*, [1312.5695](#).
- [54] A. Crivellin, F. D’Eramo and M. Procura, *New Constraints on Dark Matter Effective Theories from Standard Model Loops*, *Phys. Rev. Lett.* **112** (2014) 191304 [[1402.1173](#)].
- [55] F. D’Eramo and M. Procura, *Connecting Dark Matter UV Complete Models to Direct Detection Rates via Effective Field Theory*, *JHEP* **04** (2015) 054 [[1411.3342](#)].
- [56] F. D’Eramo, B.J. Kavanagh and P. Panci, *You can hide but you have to run: direct detection with vector mediators*, *JHEP* **08** (2016) 111 [[1605.04917](#)].
- [57] PIENU collaboration, *Improved search for heavy neutrinos in the decay $\pi \rightarrow e\nu$* , *Phys. Rev. D* **97** (2018) 072012 [[1712.03275](#)].
- [58] S. Gori et al., *Dark Sector Physics at High-Intensity Experiments*, [2209.04671](#).
- [59] V. Marra, R. Rosenfeld and R. Sturani, *Observing the dark sector*, *Universe* **5** (2019) 137 [[1904.00774](#)].
- [60] M. Deliyergiyev, *Recent Progress in Search for Dark Sector Signatures*, *Open Phys.* **14** (2016) 281 [[1510.06927](#)].
- [61] R. Hofmann, *An $SU(2)$ Gauge Principle for the Cosmic Microwave Background: Perspectives on the Dark Sector of the Cosmological Model*, *Universe* **6** (2020) 135 [[2009.03734](#)].
- [62] T. Lagouri, *Review on Higgs Hidden–Dark Sector Physics at High-Energy Colliders*, *Symmetry* **14** (2022) 1299.
- [63] ATLAS collaboration, *Search for new phenomena in events with an energetic jet and missing transverse momentum in pp collisions at $\sqrt{s} = 13$ TeV with the ATLAS detector*, *Phys. Rev. D* **103** (2021) 112006 [[2102.10874](#)].
- [64] ATLAS collaboration, *Search for a heavy charged boson in events with a charged lepton and missing transverse momentum from pp collisions at $\sqrt{s} = 13$ TeV with the ATLAS detector*, *Phys. Rev. D* **100** (2019) 052013 [[1906.05609](#)].
- [65] ATLAS collaboration, *Search for a new heavy gauge boson resonance decaying into a lepton and missing transverse momentum in 36 fb^{-1} of pp collisions at $\sqrt{s} = 13$ TeV with the ATLAS experiment*, *Eur. Phys. J. C* **78** (2018) 401 [[1706.04786](#)].

- [66] CMS collaboration, *Search for high-mass resonances in final states with a lepton and missing transverse momentum at $\sqrt{s} = 13$ TeV*, *JHEP* **06** (2018) 128 [[1803.11133](#)].
- [67] X. Cid Vidal et al., *Report from Working Group 3: Beyond the Standard Model physics at the HL-LHC and HE-LHC*, *CERN Yellow Rep. Monogr.* **7** (2019) 585 [[1812.07831](#)].
- [68] CEPC STUDY GROUP collaboration, *CEPC Technical Design Report: Accelerator*, *Radiat. Detect. Technol. Methods* **8** (2024) 1 [[2312.14363](#)].
- [69] CEPC STUDY GROUP collaboration, *CEPC Conceptual Design Report: Volume 2 - Physics \mathcal{E} Detector*, [1811.10545](#).
- [70] R.H. Helm, *Inelastic and elastic scattering of 187-mev electrons from selected even-even nuclei*, *Phys. Rev.* **104** (1956) 1466.
- [71] J.D. Lewin and P.F. Smith, *Review of mathematics, numerical factors, and corrections for dark matter experiments based on elastic nuclear recoil*, *Astropart. Phys.* **6** (1996) 87.
- [72] A.L. Fitzpatrick, W. Haxton, E. Katz, N. Lubbers and Y. Xu, *The Effective Field Theory of Dark Matter Direct Detection*, *JCAP* **02** (2013) 004 [[1203.3542](#)].
- [73] Y.V. Stadnik and V.V. Flambaum, *Nuclear spin-dependent interactions: Searches for WIMP, Axion and Topological Defect Dark Matter, and Tests of Fundamental Symmetries*, *Eur. Phys. J. C* **75** (2015) 110 [[1408.2184](#)].
- [74] SUPER-KAMIOKANDE collaboration, *Measurement of the neutrino-oxygen neutral-current quasielastic cross section using atmospheric neutrinos at Super-Kamiokande*, *Phys. Rev. D* **99** (2019) 032005 [[1901.05281](#)].
- [75] CRESST collaboration, *Results on light dark matter particles with a low-threshold CRESST-II detector*, *Eur. Phys. J. C* **76** (2016) 25 [[1509.01515](#)].
- [76] CRESST collaboration, *First results on low-mass dark matter from the CRESST-III experiment*, *J. Phys. Conf. Ser.* **1342** (2020) 012076 [[1711.07692](#)].
- [77] DARKSIDE collaboration, *First Results from the DarkSide-50 Dark Matter Experiment at Laboratori Nazionali del Gran Sasso*, *Phys. Lett. B* **743** (2015) 456 [[1410.0653](#)].
- [78] DARKSIDE collaboration, *Low-Mass Dark Matter Search with the DarkSide-50 Experiment*, *Phys. Rev. Lett.* **121** (2018) 081307 [[1802.06994](#)].
- [79] XENON collaboration, *First Dark Matter Search with Nuclear Recoils from the XENONnT Experiment*, *Phys. Rev. Lett.* **131** (2023) 041003 [[2303.14729](#)].

- [80] PANDAX collaboration, *Search for Dark-Matter–Nucleon Interactions with a Dark Mediator in PandaX-4T*, *Phys. Rev. Lett.* **131** (2023) 191002 [[2308.01540](#)].
- [81] BOREXINO collaboration, *Modulations of the Cosmic Muon Signal in Ten Years of Borexino Data*, *JCAP* **02** (2019) 046 [[1808.04207](#)].
- [82] PICO collaboration, *Dark Matter Search Results from the Complete Exposure of the PICO-60 C₃F₈ Bubble Chamber*, *Phys. Rev. D* **100** (2019) 022001 [[1902.04031](#)].
- [83] EDELWEISS collaboration, *Final results of the EDELWEISS-II WIMP search using a 4-kg array of cryogenic germanium detectors with interleaved electrodes*, *Phys. Lett. B* **702** (2011) 329 [[1103.4070](#)].
- [84] COSINE collaboration, *Development of ultra-pure NaI(Tl) detectors for the COSINE-200 experiment*, *Eur. Phys. J. C* **80** (2020) 814 [[2004.06287](#)].
- [85] LZ collaboration, *New constraints on ultraheavy dark matter from the LZ experiment*, *Phys. Rev. D* **109** (2024) 112010 [[2402.08865](#)].
- [86] SUPERCDMS collaboration, *A Search for Low-mass Dark Matter via Bremsstrahlung Radiation and the Migdal Effect in SuperCDMS*, [2203.02594](#).
- [87] SENSEI, DAMIC-M, DAMIC collaboration, *Confirmation of the spectral excess in DAMIC at SNOLAB with skipper CCDs*, *Phys. Rev. D* **109** (2024) 062007 [[2306.01717](#)].
- [88] DEAP-3600 collaboration, *Latest results from the DEAP-3600 experiment at SNOLAB*, *PoS TAUP2023* (2024) 075.
- [89] CDEX collaboration, *Projected WIMP sensitivity of the CDEX-50 dark matter experiment*, *JCAP* **07** (2024) 009 [[2309.01843](#)].
- [90] PANDAX collaboration, *Constraints on the axial-vector and pseudo-scalar mediated WIMP-nucleus interactions from PandaX-4T experiment*, *Phys. Lett. B* **834** (2022) 137487 [[2208.03626](#)].
- [91] CRESST collaboration, *Testing spin-dependent dark matter interactions with lithium aluminate targets in CRESST-III*, *Phys. Rev. D* **106** (2022) 092008 [[2207.07640](#)].
- [92] PICASSO collaboration, *Constraints on Low-Mass WIMP Interactions on ¹⁹F from PICASSO*, *Phys. Lett. B* **711** (2012) 153 [[1202.1240](#)].
- [93] J.R. Ellis and R.A. Flores, *Realistic predictions for the detection of supersymmetric dark matter*, *Nucl. Phys. B* **307** (1988) 883.

- [94] L. Girlanda, A. Kievsky and M. Viviani, *Subleading contributions to the three-nucleon contact interaction*, *Phys. Rev. C* **84** (2011) 014001 [[1102.4799](#)].
- [95] A.F. Pacheco and D. Strottman, *Nuclear Structure Corrections to Estimates of the Spin Dependent WIMP Nucleus Cross-section*, *Phys. Rev. D* **40** (1989) 2131.
- [96] J. Engel and P. Vogel, *Spin dependent cross-sections of weakly interacting massive particles on nuclei*, *Phys. Rev. D* **40** (1989) 3132.
- [97] J. Engel, M.T. Ressel, I.S. Towner and W.E. Ormand, *Response of mica to weakly interacting massive particles*, *Phys. Rev. C* **52** (1995) 2216 [[hep-ph/9504322](#)].
- [98] P.C. Divari, T.S. Kosmas, J.D. Vergados and L.D. Skouras, *Shell model calculations for light supersymmetric particle scattering off light nuclei*, *Phys. Rev. C* **61** (2000) 054612.
- [99] M.T. Ressel and D.J. Dean, *Spin dependent neutralino - nucleus scattering for A approximately 127 nuclei*, *Phys. Rev. C* **56** (1997) 535 [[hep-ph/9702290](#)].